中国光学（中英文） Chinese Optics 核心期刊

Multi-Fano resonances sensing based on a non-through metal-insulator-metal waveguide coupling D-shaped cavity

ZHAO Xiao-long, CHANG Xu-yan, LIU Yan-li, ZHANG Yan-Jun, ZHANG Zhi-dong

Citation:
ZHAO Xiao-long, CHANG Xu-yan, LIU Yan-li, ZHANG Yan-Jun, ZHANG Zhi-dong. Multi-Fano resonances sensing based on a non-through metal-insulator-metal waveguide coupling D-shaped cavity[J]. *Chinese Optics*, 2025, 18(6): 1484-1494. doi: 10.37188/CO.EN-2025-0017
赵小龙, 常旭艳, 刘艳莉, 张彦军, 张志东. 基于非连通金属介质金属波导耦合D形谐振腔的多法诺共振传感器[J]. 中国光学, 2025, 18(6): 1484-1494. doi: 10.37188/CO.EN-2025-0017

View online: https://doi.org/10.37188/CO.EN-2025-0017

Articles you may be interested in

Double Fano resonance and refractive index sensors based on parallel-arranged Au nanorod dimer metasurface arrays
基于Au纳米平行双棒超表面阵列的双Fano共振和折射率传感器特性研究
Chinese Optics. 2023, 16(4): 961 https://doi.org/10.37188/CO.EN-2023-0008

Multiple Fano resonance properties of nanoring-heptamer metal-dielectric structures
纳米环-七聚体金属-介电结构的多重Fano共振特性
Chinese Optics. 2023, 16(1): 214 https://doi.org/10.37188/CO.2022-0170

Improving sensitivity by multi-coherence of magnetic surface plasmons
通过磁表面等离激元的多重相干提高灵敏度
Chinese Optics. 2023, 16(2): 458 https://doi.org/10.37188/CO.EN.2022-0009

High-sensitivity surface plasmon resonance sensor based on the ten-fold eccentric core quasi-D-shaped photonic quasi-crystal fiber coated with indium tin oxide
基于氧化铟锡的十重偏芯D型光子准晶光纤的高灵敏度表面等离子体共振传感器
Chinese Optics. 2022, 15(1): 101 https://doi.org/10.37188/CO.EN.2021-0006

A novel methane and hydrogen sensor with surface plasmon resonance-based photonic quasi-crystal fiber
基于表面等离子体共振的光子准晶体光纤甲烷氢气传感器
Chinese Optics. 2023, 16(1): 174 https://doi.org/10.37188/CO.EN.2022-0006

Photon-assisted Fano resonance tunneling periodic double-well potential characteristics
光子辅助Fano共振隧穿周期双阱势特性
Chinese Optics. 2021, 14(5): 1251 https://doi.org/10.37188/CO.2020-0068

文章编号 2097-1842(2025)06-1484-11

Multi-Fano resonances sensing based on a non-through metal-insulator-metal waveguide coupling D-shaped cavity

ZHAO Xiao-long[1,2†], CHANG Xu-yan[1†], LIU Yan-li[1,3*], ZHANG Yan-Jun[1], ZHANG Zhi-dong[1*]

（1. *State key Laboratory of Extreme Environment Optoelectronic Dynamic Testing Technology and Instrument*, *North University of China*, *Taiyuan* 030051, *China*;

2. *School of Electrical and Control Engineering*, *North University of China*, *Taiyuan* 030051, *China*;

3. *Institute of Innovation and Entrepreneurship*, *North University of China*, *Taiyuan* 030051, *China*）

† *These authors contributed equally to this work*

* *Corresponding author*, *E-mail*: *liuyanli*0561@126.*com*; *zdzhang@nuc.edu.cn*

Abstract: A plasmonics waveguide structure that consist of a non-through metal–insulator–metal (MIM) waveguide coupled with a D-shaped cavity was designed. And the transmission properties, magnetic field distribution, and refractive index sensing functionality were simulated using the finite element method (FEM). A multi-Fano resonance phenomenon was clearly observable in the transmission spectra. The Fano resonances observed in the proposed structure arise from the interaction between the discrete states of the D-shaped resonant cavity and the continuum state of the non-through MIM waveguide. The influence of structural parameters on Fano resonance modulation was investigated through systematic parameter adjustments. Additionally, the refractive index sensing properties, based on the Fano resonance, were investigated by varying the refractive index of the MIM waveguide's insulator layer. A maximum sensitivity and FOM of 1 155 RIU/nm and 40 were achieved, respectively. This research opens up new possibilities for designing and exploring high-sensitivity photonic devices, micro-sensors, and innovative on-chip sensing architectures for future applications.

Key words: surface plasmon polaritons; metal-insulator-metal (MIM) waveguide; D-shaped resonant cavity; double Fano resonance; refractive index sensor

收稿日期:2025-03-06; **修订日期**:2025-03-13

基金项目:山西省重点研发计划项目（No. 202102020101010）

Supported by Key Research and Development Program of Shanxi Province (No. 202102020101010)

基于非连通金属–介质–金属波导耦合 D 形谐振腔的多法诺共振传感器

赵小龙[1,2†], 常旭艳[1†], 刘艳莉[1,3*], 张彦军[1], 张志东[1*]
(1. 中北大学 极限环境光电测试技术与仪器全国重点实验室, 山西 太原 030051;
2. 中北大学 电气与控制工程学院, 山西 太原 030051;
3. 中北大学 创新创业学院, 山西 太原 030051)
† 共同第一作者

摘要: 本文设计了一种由两个一端封堵的金属-绝缘体-金属(MIM)波导与一个 D 形腔耦合组成的表面等离激元波导结构。使用有限元方法(FEM)模拟了该结构的传输特性、磁场分布以及折射率传感特性。在透射光谱中可以明显观察到多 Fano 共振现象。这些 Fano 共振源于 D 形谐振腔产生的共振离散态与一端封堵的 MIM 波导产生的连续态之间的相互耦合。通过系统地调整结构参数, 研究了其对 Fano 共振调制的影响。此外, 通过改变 MIM 波导中绝缘层的折射率, 研究了基于 Fano 共振折射率传感特性。结果表明, 该结构实现的最大折射率灵敏度和品质因子(FOM)分别为 1 155 RIU/nm 和 40。这些研究对高灵敏度光子器件、微型传感器、未来新型片上传感的设计和研究提供了新的途径。

关 键 词: 表面等离激元; 金属-绝缘体-金属波导; D 形谐振腔; 双 Fano 共振; 折射率传感器
中图分类号: O482.31 **文献标志码:** A **doi:** 10.37188/CO.EN-2025-0017 **CSTR:** 32171.14.CO.EN-2025-0017

1 Introduction

Surface plasmon polaritons (SPPs) are collective oscillation modes that emerge from the interaction between incident light and free electrons at a metal-dielectric interface. These SPPs propagate along the metal surface while decaying exponentially in the perpendicular direction[1-3]. Consequently, electromagnetic energy becomes tightly confined to the metal surface[4-5], allowing SPPs to surpass the optical diffraction limit[6]. This unique property has led to the discovery and realization of numerous special optical phenomena, devices, and applications based on SPPs[7-8].

As the simplest waveguides for propagating SPPs, Metal-Insulator-Metal (MIM) waveguides have garnered extensive attention, facilitating the design of various photonic devices such as filters, sensors, isolators, and more[9-11]. In particular, highly sensitive sensors based on MIM waveguide-coupled resonators have been intensively studied in recent years. It has been found that incorporating photonic structures capable of realizing discrete and continuous states can significantly enhance sensor sensitivity through nonlinear Fano resonance[12-14].

Fano resonance, characterized by its weak coupling nature, exhibits extreme sensitivity to changes in structural parameters and the surrounding dielectric environment[15-16]. This sensitivity, combined with the asymmetric line shape of Fano resonance[17-18], makes it particularly attractive for sensing applications. It has significant applications in various fields, including biosensing, surface-enhanced Raman scattering (SERS), nonlinear optical devices, high-performance photoelectric sensing, optical filters, all-optical switches, and photonic sensors. Therefore, researchers have shown great interest in exploring various configurations of MIM waveguide-coupled resonator systems to optimize sensor performance and simplify sensor structure[19-20]. MIM waveguide coupled resonator structures hold significant potential in the field of nanophotonics. However, their development still requires overcoming challenges such as high losses, coupling light to these nanoscale waveguides, fab-

rication precision, and thermal effects. Through structural innovation, optimized design, and improvements in fabrication techniques, it is anticipated that high-performance, low-loss, and tunable integrated photonic devices can be achieved in the future, thereby facilitating the practical application of nanophotonic technologies[21-23].

In this paper, we present a multi-Fano resonance plasmonic sensing system that combines a non-through MIM waveguide with a D-shaped cavity for generating multiple Fano resonances. The transmission spectrum and magnetic field distributions of the system were simulated using the finite element method (FEM). The generation mechanisms of these distinct Fano resonances were explored by analyzing the steady-state magnetic field distributions at each resonance wavelength. Furthermore, we discussed how variations in geometric parameters influence the Fano resonances and investigated the sensing performance based on these resonances. Additionally, the sensitivity for each of the distinct Fano resonance peaks is presented and analyzed.

2 Structure model and analytical method

The 2D schematic of the plasmonic sensing system is shown in Fig. 1 (color online), the system consists of a non-through MIM waveguide coupled with a D-shaped cavity. The D-shaped resonant cavity is characterized by an asymmetric structure, which is structurally simple and easy to process. In Fig. 1, the green and white regions represent Ag (ε_m) and air (ε_s), respectively. The widths of both the MIM waveguides and the D-shaped ring are fixed at 50 nm to support only the fundamental transverse magnetic mode (TM_0). The length of each non-through MIM waveguide is denoted by L, while the gap between the two non-through MIM waveguides is represented by d. The distance between the D-shaped cavity and the non-through MIM waveguide is denoted by g. The inner and outer radii of the D-shaped cavity are denoted as R_1 and R_2, respectively, with the center radius of the ring cavity calculated as $r = (R_1+R_2)/2$. Additionally, l represents the vertical height increase of the horizontal part of the D-shaped cavity.

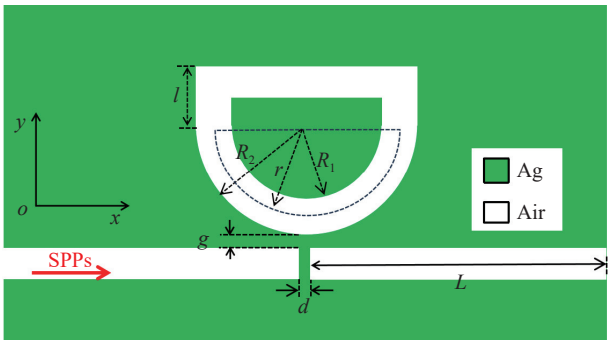

Fig. 1 Two-dimensional schematic for the non-through MIM waveguide and a D-shaped cavity

The frequency-dependent complex relative permittivity $\varepsilon(\varpi)$ of silver is characterized by the modified Debye–Drude dispersion mode[3, 24] as follows:

$$\varepsilon(\varpi) = \frac{\varepsilon_\infty + (\varepsilon_s - \varepsilon_\infty)}{1 + i\varpi\tau} + \frac{\sigma}{i\varpi\varepsilon_0} \quad , \qquad (1)$$

where $\varepsilon_\infty = 3.8344$ is the infinite frequency permittivity, $\varepsilon_s = -9\,530.5$ represents the static permittivity, $\sigma = 1.1486 \times 10^7$ S/m is the conductivity, and $\tau = 7.35 \times 10^{-15}$ s is the relaxation time.

The transmission properties of the non-through MIM waveguide coupled with a D-shaped cavity are investigated by using the FEM with perfectly matched layer absorbing boundary condition. The left and right ends of the proposed structure are configured with numerical ports, with the left end open and the right end closed. The transmittance is defined as $T = |S_{21}|^2$, where S_{21} is the transmittance of the MIM waveguide[25].

The width of the MIM waveguide and the D-shaped cavity is fixed to 50 nm, which can only support the fundamental transverse magnetic (TM_0) mode pass in the MIM waveguide. The dispersion relation of the TM_0 mode can be expressed as[26]

$$\tanh(\kappa w) = -2\kappa p\alpha/(\kappa^2+p^2\alpha^2) \quad , \qquad (2)$$

where κ and w are the perpendicular core wave vec-

tor and the insulator width of the MIM waveguide, respectively. The symbols in Eq. (1) are defined as $p = \varepsilon_{in}/\varepsilon_m$ and $\alpha = [k_0^2(\varepsilon_{in}-\varepsilon_m)+\kappa]^{1/2}$. ε_{in} and ε_m are the dielectric constants of the insulator and the metal, respectively; $k_0 = 2\pi/\lambda_0$ is the free space wave vector; κ can be solved from Ref. [27] by using the iterative method. Thus, the effective index n_{eff} of the MIM waveguide can be defined as $n_{eff} = (\varepsilon_m + (\kappa/k_0)^2)^{1/2}$. The wavelength of SPPs, λ_{spp}, can be expressed as $\lambda_{spp} = \lambda_0/\mathrm{Re}(n_{eff})$, where Re ($n_{eff}$) is the real part of n_{eff}.

3 Results and discussion

The transmission spectrum and steady-state magnetic field distribution of the target structure were analyzed using COMSOL Multiphysics simulation software, and the optical properties of the target structure were discussed in detail. Figure 2 (color online) illustrates the transmission spectra for three configurations: a standalone non-through waveguide, a through waveguide coupled with a D-shaped cavity, and a non-through waveguide coupled with a D-shaped cavity (proposed structure), using parameters d = 10 nm, g = 10 nm, R_1 = 100 nm, R_2 = 150 nm and $r_2 = (R_1+R_2)/2$=125 nm, l = 140 nm. For the standalone non-through waveguide, a broad spectral resonance peak is observed (black solid line). In contrast, the through waveguide coupled with the D-shaped cavity exhibits three distinct transmission troughs (red solid line). The proposed structure, featuring a non-through waveguide coupled with a D-shaped cavity, shows three distinct Fano resonance peaks in the transmission spectrum (blue solid line). The transmission spectrum reveals three narrow transmission dips of the through waveguide coupled with a D-shaped cavity at wavelengths l_1 = 1.185 μm, l_2 = 0.595 μm, and l_3 = 0.445 μm, which can be considered as discrete states. The broad spectral resonance peak of the non-through MIM waveguide represents a continuum state. Consequently, the Fano resonances observed in the proposed structure arise from the interaction between the discrete states of the D-shaped resonant cavity and the continuum state of the non-through MIM waveguide.

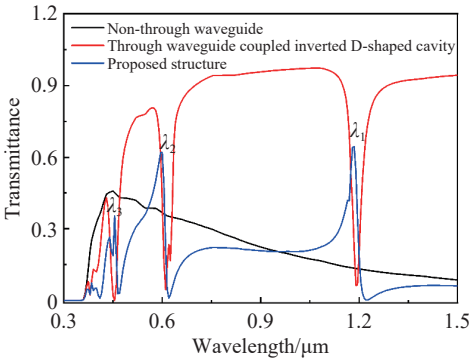

Fig. 2 Transmission spectra for three distinct configurations

To elucidate the physical mechanism of Fano resonance in the proposed structure, the normalization Hz field distributions at the Fano resonance peak (λ = 0.455 μm, 0.595 μm, and 1.185 μm,) and dip (λ = 0.465 μm, 0.62 μm, and 1.22 μm) are calculated and showed in Fig. 3(a)–(f) (color online). For λ= 0.455 μm (Fig. 3(a)), the real part of the effective refractive index (Re(n_{eff})) is 1.55, and the SPP wavelength (l_{SPPs}) is 293 nm. Consequently, the number of modes in the D-shaped resonator is 2.98, which is calculated by dividing its length (872.5 nm) by the SPP wavelength (293 nm). So, three stable magnetic fields patterns form in the D-shaped resonator. This theoretical prediction shows excellent consistency with the simulated field distribution in Fig. 3(a). A stable mode distribution forms within the incident waveguide and the D-shaped resonator, with concentrated magnetic field energy regions near the right end of the incident waveguide, the left end of the outgoing waveguide, and the bottom end of the resonator. Most of the SPP energy is coupled into the D-shaped resonator, with some coupling into the exit waveguide. In contrast, for λ= 0.465 μm, (Fig. 3(b)), the real part of the effective refractive index (Re(n_{eff})) is 1.54, and the SPP wavelength (l_{SPPs}) is 302 nm, almost all SPP energy couples into the D-shaped resonator, with negli-

gible coupling to the exit waveguide. Consequently, in Fig. 2, the transmission coefficient of its corresponding Fano resonance peak is approximately 0.4, while the transmission coefficient at its transmission dip is close to 0. For the transmission peak at λ= 0.595 μm, and the dip λ = 0.62 μm (Fig. 3(c) and 3(d)), the real part of the effective refractive index (Re(n_{eff})) is 1.46 and 1.45, and the SPP wavelength (l_{SPPs}) is 408 nm and 428 nm. The number of modes of the transmission peak at λ= 0.595 μm in the D-shaped resonator is 2.14. Two stable magnetic fields patterns form in the D-shaped resonator. The SPP energy excited by the transmission peak wavelength couples more strongly into the exit waveguide compared to Fig. 3(a). For the transmission valley wavelength, minimal SPP energy is generated in the incident waveguide, and almost no energy couples into the exit waveguide or the resonator. At the transmission peaks and dips (λ= 1.185 μm, and λ= 1.22 μm, shown in Fig. 3(e) and 3(f)), the real part of the effective refractive index (Re(n_{eff})) is 1.396 and 1.395, and the SPP wavelength (l_{SPPs}) is 849 nm and 874 nm. The number of modes of the transmission peak at λ= 0.595 μm in the D-shaped resonator is 1.03. One stable magnetic field pattern forms within the D-shaped cavity, concentrating SPP energy. For the transmission peak wavelength, wave nodes form at the right end of the incident waveguide, the left end of the exit waveguide, and the bottom of the resonator. At the transmission valley wavelength, wave nodes form at the right end of the incident waveguide and the bottom of the resonator, resulting in nearly all SPPs coupling into the D-shaped cavity.

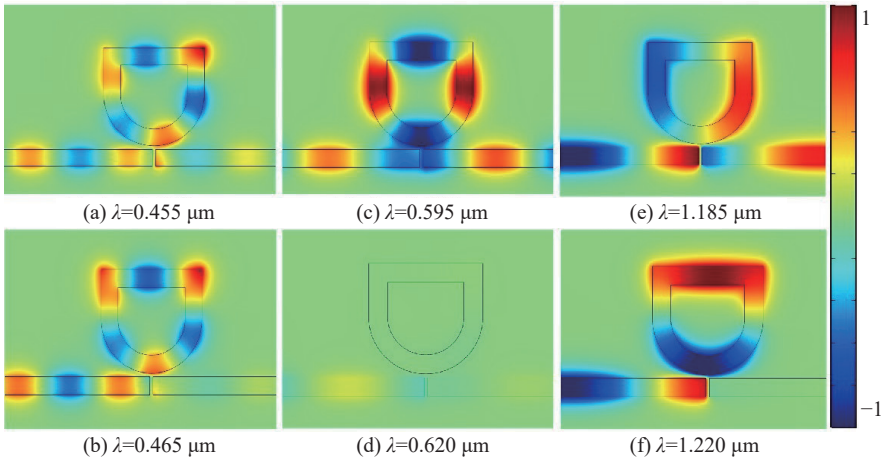

Fig. 3 Contour profiles of the normalized Hz field distributions of the non-through MIM waveguide D-shape cavity. (a) λ = 0.455 μm, (b) λ = 0.465 μm, (c) λ = 0.595 μm, and (d) λ =0.62 μm, (e) λ = 1.185 μm, and (f) λ =1.22 μm

To investigate the influence of the D-shaped cavity on the Fano resonance, we systematically calculated transmission spectra while varying the value of r from 105 nm to 145 nm in increments of 10 nm, while keeping d and g at 10 nm. The transmission spectra are shown in Fig. 4(a) (color online). We can observe a multi-Fano resonance phenomenon within the transmission spectra. As r increases, significant redshift is observed in all three Fano resonance peaks, and compared to the other two, the redshift of the first-order Fano resonance peak is more pronounced, as shown in Fig. 4(b) (color online). Meanwhile, the second-order and third-order Fano resonance peaks also exhibit a minor redshift with increasing r. This behavior can be attributed to the fact that the first-order, second-order, and third-order Fano resonance peaks are associated with the first-order, second-order, and third-order resonant modes of the D-shaped resonant cavity, respectively. This is because the first Fano resonance peak is generated by the first-order resonance mode of the D-shaped resonant cavity. Compared to higher-order vibration modes, the first-order vibration mode is more sensitive to changes in

structural parameters. However, an interesting trend emerges regarding the transmission coefficients: as r increases, the transmission coefficient corresponding to the first-order Fano resonance peak diminishes, whereas those of the second-order and third-order Fano resonance peaks progressively strengthen. Moreover, an additional resonance peak appears on the left side of the third-order Fano resonance peak, adding complexity to the resonance spectrum. This emergent peak suggests that changes in r not only affect the existing resonant modes but also introduce new ones into the system.

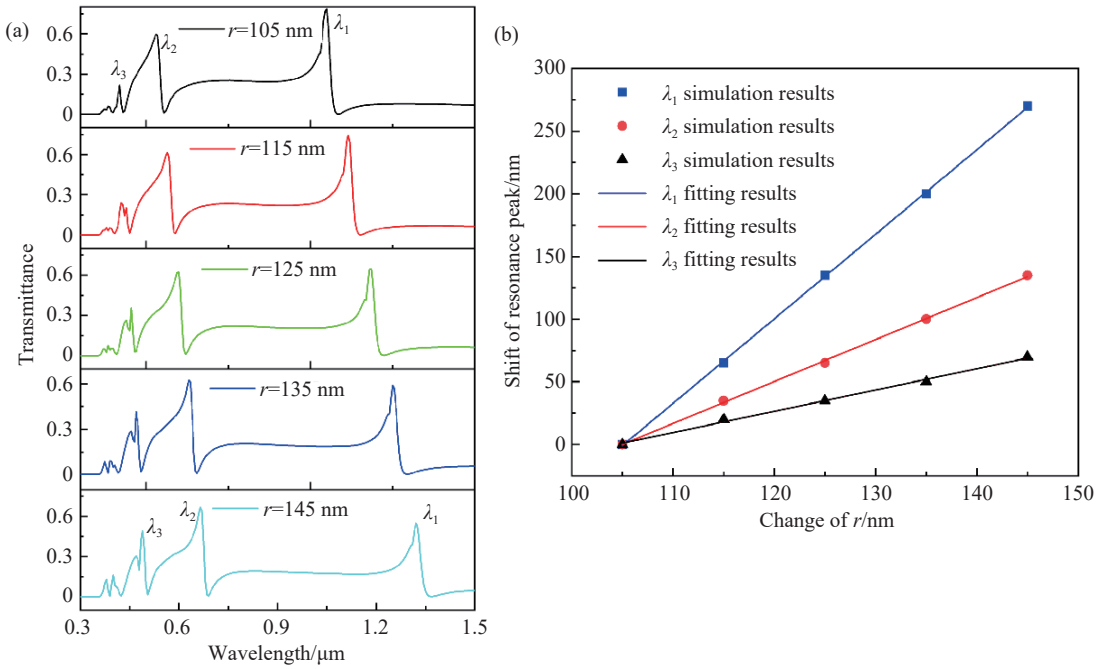

Fig. 4 (a) Transmission spectra of the non-through MIM waveguide D-shape cavity with changing r; (b) the shift of resonance peak with changing r

The transmission spectra were calculated by varying the value of l from 120 nm to 160 nm in increments of 10 nm, as shown in Fig. 5(a) (color online). A redshift phenomenon can be observed distinctly for the first-order, second-order, and third-order Fano resonance peaks as the parameter l increases from the figure 5(b) (color online). This can be attributed to the fact that the wavelengths of these three Fano resonance peaks are predominantly determined by the perimeter of the D-shaped resonant cavity. So, the circumference of the D-shaped cavity increases with the increase of l, which results in the Fano resonance peaks redshift. And the redshift rate of the first-order Fano resonance peak is greater than that of the second-order Fano resonance peak as increase of l.

The impact of the gap g between the MIM waveguide and the D-shaped resonant cavity on the transmission characteristics of the coupled resonant system is investigated by varying g from g = 10 nm to g = 30 nm with an increment of 5nm, with the spectra shown in Fig. 6(a) (color online). We found that when g increases from 10 nm to 15 nm, all three Fano resonance peaks undergo significant blueshift. This is because an increase in g allows plasmon waves with a larger skin depth to couple well into the D-shaped resonant cavity. The skin depth is

$$\delta_c = 1/\alpha, \quad \alpha = \omega\sqrt{\mu\varepsilon\sec\delta\sin(\delta/2)} \quad ,$$

where δ is loss tangent, and it is inversely proportional to the frequency of the plasmon waves ω. Therefore, the increase of the coupling distance leads to blueshift of the resonance peaks. For g increasing from 15 nm to 30 nm, the three resonance peaks hardly shift as shown in Fig. 6(b) (color online). This is because at g = 15 nm, the skin depth

$\delta_c > g$ corresponds to the resonance peak wavelengths. However, the transmission coefficient of the first-order Fano resonance peak significantly decreases at g = 30 nm.

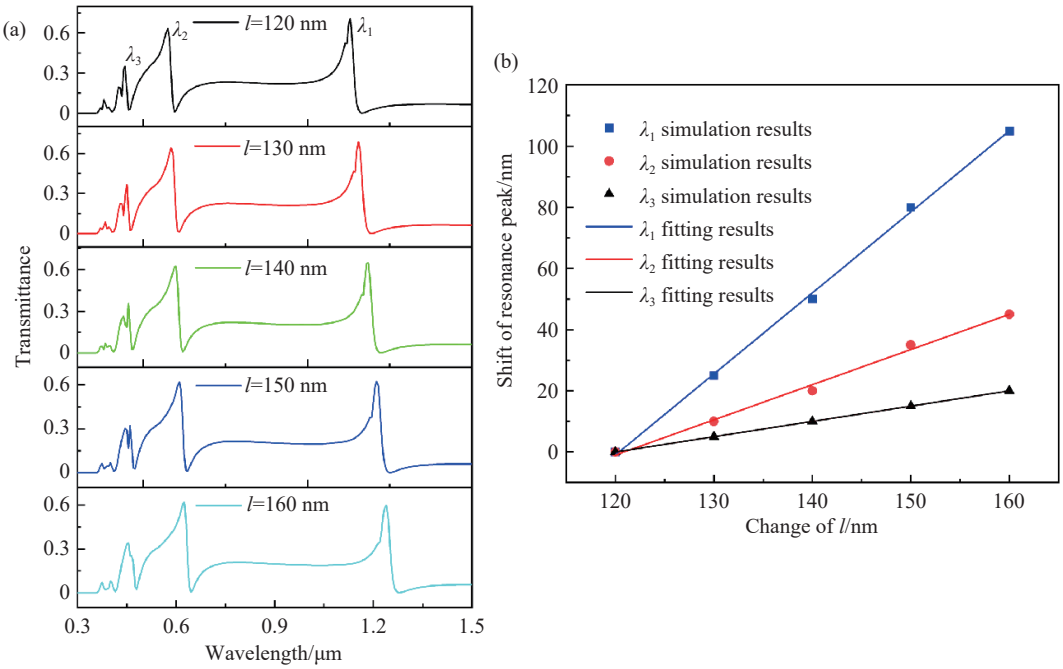

Fig. 5 (a) Transmission spectra of the non-through MIM waveguide D-shape cavity with changing l; (b) the shift of resonance peak with changing l

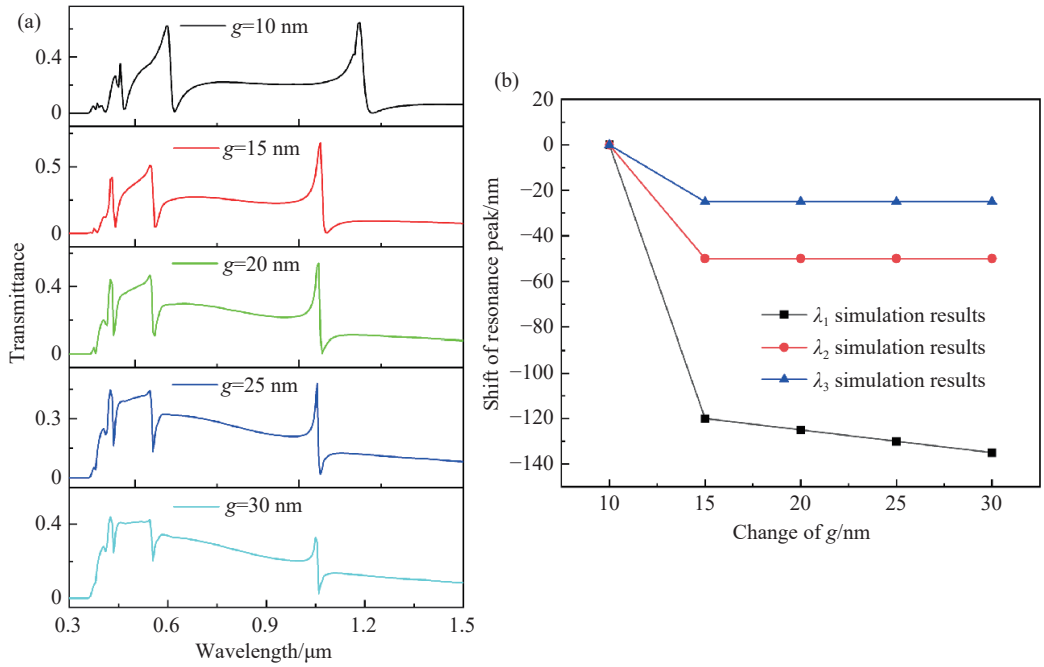

Fig. 6 (a) Transmission spectra of the non-through MIM waveguide D-shape cavity with changing g; (b) the shift of resonance peak with changing g

The transmission spectra were calculated by varying the value of d from 10 nm to 30 nm in increments of 5 nm, as shown in Fig. 7(a) (color online). The transmission peak as a function of the distance d between two MIM waveguides is displayed in the figure 7(b) and (c) (color online). Evidently,

as d increases, the Fano resonance peak position remains stable, and its transmission coefficient shows no significant variation (Fig. 7a). This is because the SPP waves do not couple directly from the incident waveguide to the outgoing waveguide through the gap between them. Instead, the SPPs of the incident waveguide first couple to a D-shaped resonant cavity, where resonance occurs, and then couple to the outgoing waveguide. Additionally, in the transmission spectrum at d = 10 nm, a new resonance peak is observed on the left side of the third-order Fano resonance peak. This resonance peak gradually becomes more pronounced as d increases and undergoes a blue shift, separating from the third-order Fano resonance peak. This is because the energy is primarily transferred through direct coupling between the two waveguides when the spacing d between SPPs is small. As d increases, the energy of this resonance peak is more often transmitted via an incident waveguide through a D-shaped resonator and then coupled into the outgoing waveguide. Therefore, when d >15 nm, a significant blue shift is observed in this resonance peak, meaning the resonance frequency shifts to a higher frequency.

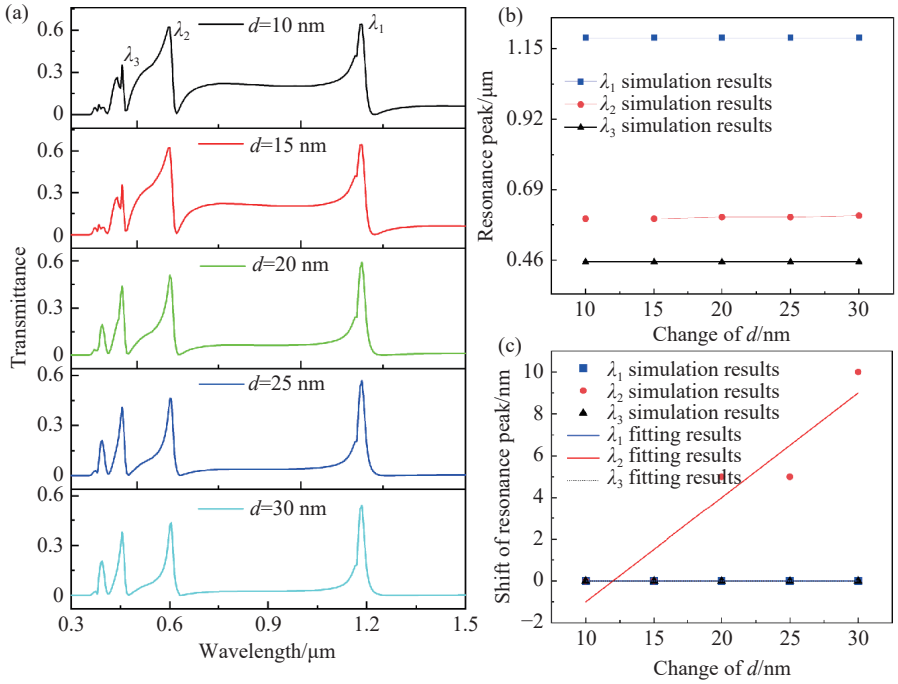

Fig. 7 (a) Transmission spectra of the non-through MIM waveguide D-shape cavity with changing d; (b) the relationship between the resonance peak with changing d, and (c) the shift of resonance peak with changing d

Fig. 8 (color online) presents the transmission spectra for different dielectric materials in a MIM waveguide. As shown in figs. 8(a) and (b), we found that three Fano resonant peaks redshift as the refractive index increases, demonstrating a significant sensitivity to changes in the environmental refractive index. Figure 8(b) presents the relationship between the variations in refractive index and the three Fano resonance peaks (λ_1, λ_2, and λ_3). We found that the first-order Fano resonance peak is more sensitive to changes in refractive index than the second-order and third-order Fano resonance peaks. To further quantitatively evaluate the sensitivity characteristics of the refractive index sensor based on the Fano resonance, the sensitivity S and the figure of merit (FOM) are used to characterize the sensitivity. The sensitivity $S = \delta_\lambda/\delta_n$, and the $FOM = \Delta T/T\Delta n$, where $T = 0.5\times[T(n = 1.00) + T(n = 1.02)]$, and the $FOM^* = max\ |FOM|$, Where δ_λ is the changes of the Fano resonance peak, and the δ_n is corresponding changing the environmental refractive index, and the FWHM is Full Width at Half

Maximum of the Fano resonance peak. The maximum refractive index sensitivities S and the FOM^* are 1 155 nm/RIU and 40, respectively.

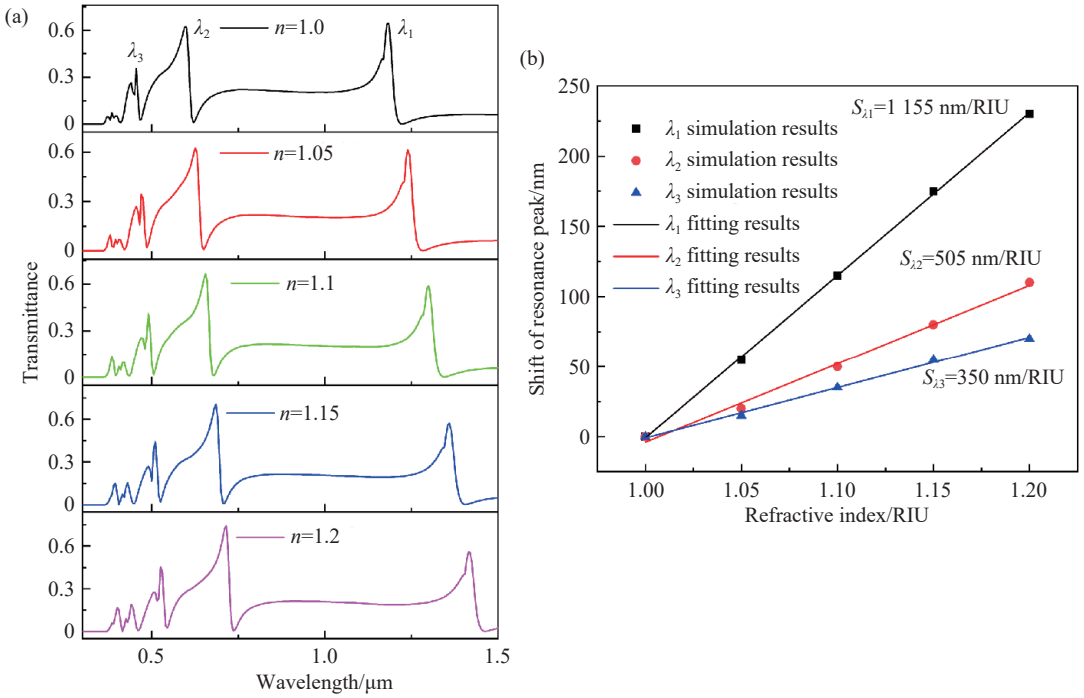

Fig. 8 (a) Transmission spectra of the non-through MIM waveguide-coupled D-shape cavity with changing n; (b) shift of the Fano resonance peak as a function of the refractive index change n

4 Conclusion

In this work, we propose a plasmonic structure consisting of a D-shaped cavity coupled to a MIM waveguide, and numerically simulate its transmission properties using the FEM. A multi-Fano resonance phenomenon is observed in the MIM waveguide coupled to the D-shaped cavity. By analyzing the steady-state magnetic field distribution excited by wavelengths corresponding to different Fano resonance modes, we investigate the generation mechanisms of these various Fano resonances. Results indicate that the multi-Fano resonances arise from the coupling of different resonance modes in the D-shaped cavity with the transmission modes of the MIM waveguide. By studying the transmission spectra under various structural parameters, we demonstrate the regulatory effects of these parameters on the Fano resonance. Furthermore, we investigate refractive index sensing based on the Fano resonance by altering the refractive index of the insulator in the MIM waveguide, achieving a maximum sensitivity of 1 155 RIU/nm and a FOM^* of 40. This study provides valuable insights for the design of new high-sensitivity photonic devices and microsensors. The two-dimensional planar structure designed in this study can be fabricated using standard micro-nano fabrication processes. The specific procedure is as follows: firstly, a photoresist layer is spin-coated onto a silicon substrate, followed by patterning using photolithography; subsequently, a silver film is deposited via magnetron sputtering; finally, the target structure is obtained after a photoresist removal and cleaning step. This fabrication process is mature and reliable, compatible with existing micro-nano fabrication technologies, and demonstrates excellent experimental feasibility.

References:

[1] ZAYATS A V, SMOLYANINOV I I. Near-field photonics: surface plasmon polaritons and localized surface

plasmons[J]. *Journal of Optics A: Pure and Applied Optics*, 2003, 5(4): S16-S50.

[2] 裴佳欢, 齐小花, 邹明强, 等. 表面增强拉曼光谱在动物源性食品兽药残留检测的研究进展[J]. 应用化学, 2024, 41(4): 459-471.
PEI J H , QI X H, ZOU M Q, *et al*.. Advances in Surface-Enhanced Raman Spectroscopy for the Detection of Veterinary Drug Residues in Foods of Animal Origin[J]. *Chinese Journal of Applied Chemistry*, 2024, 41(4): 459-471. (in Chinese).

[3] 刘镜, 刘娟, 王涌天, 等. 亚波长金属光栅的表面等离子体激元共振特性[J]. 中国光学, 2011, 4(4): 363-368.
LIU J, LIU J, WANG Y T, *et al*.. Resonant properties of sub-wavelength metallic gratings[J]. *Chinese Optics*, 2011, 4(4): 363-368. (in Chinese).

[4] 陈韶云, 张行颖, 刘奔, 等. 表面增强拉曼光谱基底的种类及其应用进展[J]. 分析化学, 2024, 52(7): 910-924.
CHEN S Y, ZHANG X Y, LIU B, *et al*.. Classification and Application of Surface-enhanced Raman Spectroscopy Substrates[J]. *Chinese Journal of Analytical Chemistry*, 2024, 52(7): 910-924. (in Chinese).

[5] 龚宏波, 胡伟晔, 黄秋婷, 等. 基于表面增强拉曼光谱技术对负电性分子的高灵敏定性分析[J]. 分析化学, 2023, 51(7): 1213-1221.
GONG H B, HU W Y, HUANG Q T, *et al*.. Highly Sensitive Qualitative Analysis of Electronegative Molecules Based on Surface-enhanced Raman Spectroscopy[J]. *Chinese Journal of Analytical Chemistry*, 2023, 51(7): 1213-1221. (in Chinese).

[6] 朱君, 李志全. Otto 结构加载 MIM 波导的表面等离子激元传输与衰减特性[J]. 发光学报, 2013, 34(11): 1533-1537.
ZHU J, LI Z Q. Characteristics of transmission and attenuation of surface plasmon polaritons in Otto structure loaded MIM wave guide[J]. *Chinese Journal of Luminescence*, 2013, 34(11): 1533-1537. (in Chinese).

[7] LI M, CUSHING S K, WU N Q. Plasmon-enhanced optical sensors: a review[J]. *Analyst*, 2015, 140(2): 386-406.

[8] 雷建国, 刘天航, 林景全, 等. 表面等离子体激元的若干新应用[J]. 中国光学与应用光学, 2010, 3(5): 432-439.
LEI J G, LIU T H, LIN J Q, *et al*.. New applications of surface plasmon polaritons[J]. *Chinese Journal of Optics and Applied Optics*, 2010, 3(5): 432-439. (in Chinese).

[9] 岳斯琦, 莫展豪, 赵俊琪, 等. 基于表面增强拉曼散射特征峰位移检测触珠蛋[J]. 分析化学, 2024, 52(2): 231-239.
YUE S Q, MO Z H, ZHAO J Q, *et al*.. Detection of Haptoglobin by Surface-Enhanced Raman Scattering Based on the Shift of Characteristic Peak[J]. *Chinese Journal of Analytical Chemistry*, 2024, 52(2): 231-239. (in Chinese).

[10] 洪乐, 董伟男, 武振楠, 等. 金属纳米团簇的光响应行为在生物诊疗中的应用[J]. 应用化学, 2024, 41(9): 1238-1247.
HONG L, DONG W N, WU Z N, *et al*.. Application of Photoresponsive Behavior of Metal Nanoclusters in Biomedical Diagnostics and Therapy[J]. *Chinese Journal of Applied Chemistry*, 2024, 41(9): 1238-1247. (in Chinese).

[11] BUTT M A. Review of innovative cavity designs in metal–insulator-metal waveguide-based plasmonic sensors[J]. *Plasmonics*, 2024, 20(6): 4257-4276.

[12] CHEN J J, GAN F Y, WANG Y J, *et al*.. Plasmonic sensing and modulation based on fano resonances[J]. *Advanced Optical Materials*, 2018, 6(9): 1701152.

[13] KONG Y, CAO J J, QIAN W C, *et al*.. Multiple Fano resonance based optical refractive index sensor composed of micro-cavity and micro-structure[J]. *IEEE Photonics Journal*, 2018, 10(6): 6804410.

[14] BORETTI A. A perspective on the use of perovskite luminophores for solar windows[J]. *Advanced Sensor and Energy Materials*, 2024, 3(1): 100060.

[15] 舒杨, 杨曼, 李志豪, 等. 基于金纳米粒子聚集与杂交链式扩增的 microRNA 传感[J]. 应用化学, 2024, 41(1): 109-117.
SHU Y, YANG M, LI Z H, et, al. MicroRNA Sensing Based on Gold Nanoparticle Aggregation and Hybridization Chain Amplification[J]. *Chinese Journal of Applied Chemistry*, 2024, 41(1): 109-117. (in Chinese).

[16] GUO H Y, FANG W J, PANG J L, *et al*.. Multiple Fano resonances based on all-dielectric metastructure for refractive index sensing[J]. *Infrared Physics & Technology*, 2024, 139: 105284.

[17] ROHIMAH S, TIAN H, WANG J F, *et al*.. Fano resonance in the plasmonic structure of MIM waveguide with r-shaped resonator for refractive index sensor[J]. *Plasmonics*, 2022, 17(4): 1681-1689.

[18] 张志东, 张慧男, 梁洁, 等. 基于 Au 纳米平行双棒超表面阵列的双 Fano 共振和折射率传感器特性研究[J]. 中国光学 (中英文), 2023, 16(4): 961-971.

ZHANG Z D, ZHANG H N, LIANG J, *et al*.. Double Fano resonance and refractive index sensors based on parallel-arranged Au nanorod dimer metasurface arrays[J]. *Chinese Optics*, 2023, 16(4): 961-971. (in Chinese).

[19] ZHU J, WU C S. Optical refractive index sensor with Fano resonance based on original MIM waveguide structure[J]. *Results in Physics*, 2021, 21: 103858.

[20] RAHAD R, HOSSAIN N, HOSSAIN A. Enhanced alcohol detection using surface plasmon polariton dependent MIM plasmonic sensor[J]. *Plasmonics*, 2025, 20: 1331-1340.

[21] BUTT M A, KAZANSKIY N L, KHONINA S N. Tapered waveguide mode converters for metal-insulator-metal waveguide plasmonic sensors[J]. *Measurement*, 2023, 211: 112601.

[22] BUTT M A, PIRAMIDOWICZ R. Orthogonal mode couplers for plasmonic chip based on metal–insulator–metal waveguide for temperature sensing application[J]. *Scientific reports*, 2024, 14(1): 3474.

[23] BUTT M A. Plasmonic sensors based on a metal–insulator–metal waveguide—what do we know so far[J]. *Sensors*, 2024, 24(22): 7158.

[24] 向宪昕, 孙华悦, 柴会宁, 等. 基于智能手机的可视化生物传感器在即时检测中的研究进展[J]. 分析化学, 2024(2): 145-156.
XIANG X X, SUN H Y, CHAI H N, *et al*.. Advances in smartphone-based visual biosensors for immediate detection[J]. *Analytical Chemistry*, 2024(2): 145-156. (in Chinese).

[25] ZHANG Z D, LUO L, XUE C Y, *et al*.. Fano resonance based on metal-insulator-metal waveguide-coupled double rectangular cavities for plasmonic nanosensors[J]. *Sensors*, 2016, 16(5): 642.

[26] ZHANG Z Y, WANG J D, ZHAO Y N, *et al*.. Numerical investigation of a branch-shaped filter based on metal-insulator-metal waveguide[J]. *Plasmonics*, 2011, 6(4): 773-778.

[27] KEKATPURE R D, HRYCIW A C, BARNARD E S, *et al*.. Solving dielectric and plasmonic waveguide dispersion relations on a pocket calculator[J]. *Optics Express*, 2009, 17(26): 24112-24129.

Author Biographies:

ZHAO Xiao-long (1986—), male, born in Heishan, Liaoning Province, Doctor, associate professor, received her PhD degree from North University of China. He is an Associate Professor in the School of Electrical and Control Engineering of North University of China. His current research interests include micro/nano-photonics sensors. E-mail: zhaoxiaolong@nuc.edu.cn.

CHANG Xu-yan (2000—), female, born in Xinzhou, Shanxi Province. She is a current master's student at North China University, majoring in Instrumentation Engineering. E-mail: 1927744674@qq.com

LIU Yan-li (1985—), female, born in huaibei, Anhui Province, Doctor, associate professor, received her PhD degree from North University of China. She is an Associate Professor in the School of Information and Communication Engineering, of North University of China. Her current research interests include micro/nano-photonics. E-mail: 565347436@qq.com

ZHANG Zhi-dong (1985—), male, born in Jingle, Shanxi Province, Doctor, Professor, graduate student supervisor, received his PhD from Southwest Jiaotong University. He is currently an Professor in the school of Instrumentation and Electronics of North University of China. His research interests include micro/nano-sensors and nanophotonics. E-mail: zdzhang@nuc.edu.cn.